Non-dissipative martensitic phase transformation after multi-million superelastic cycles

Mostafa Karami,[1] Zeyuan Zhu,[1] Ka Hung Chan,[1,2]

Peng Hua,[1] Nobumichi Tamura,[2] and Xian Chen[1,*]

[1]*Department of Mechanical and Aerospace Engineering,*

The Hong Kong University of Science and Technology,

Clear Water Bay, Kowloon, Hong Kong

[2]*Advanced Light Source, Lawrence Berkeley National Laboratory, California, United States*

Abstract

Superelastic alloys used for stents, biomedical implants, and solid-state cooling devices rely on their reversible stress-induced martensitic transformations. These applications require the alloy to sustain high deformability over millions of cycles without failure. Here we report an alloy capable of enduring 10 million tensile stress-induced phase transformations while still exhibiting over 2% recoverable elastic strains. After millions of cycles, the alloy is highly reversible with zero stress hysteresis. We show that the major martensite variant is reversible even after multimillions of cycles under tensile loadings with a highly coherent $(1\bar{1}0)_A$ interface. This discovery provides new insights into martensitic transformation, and may guide the development of superelastic alloys for multi-million cycling applications.

Alloys that undergo reversible solid-solid phase transformations possess a wide range of functionalities, such as shape memory effect, superelasticity, caloric cooling, sensing and actuation. The memory effect is achieved by thermally driven phase transformation, while many other functionalities are achieved by stress-induced phase transformation. These alloys are commonly known as shape memory alloys, used for smart actuators [1]. They are also known as superelastic materials for their ability to recover large deformations under the stress-induced phase transformation, widely applied in biomedical engineering, e.g., orthodontic wires and cardiovascular stents [2, 3], and energy science, e.g., solid-state refrigerators [4, 5]. The emerging applications of these alloys require the recoverable strains to sustain over multi-millions stress-induced phase transformation cycles. Unfortunately, very rare transforming materials meet this requirement. The primary reason for the gradual loss of phase reversibility during cyclic transformations is the lattice mismatch at the interface between austenite and martensite. Under the cyclic stress-induced phase transformation, the recoverable strain degrades quickly, and strain hardening becomes prominent. For example, the most widely used shape memory alloy, Nitinol can only sustain 100 tensile cycles and 1000 compressive cycles [6–8]. The fatigue life of Nitinol can be improved by microstructure engineering, such as grain refinement and morphological manipulation [9, 10], but these treatments cause severe local amorphization [10] and lattice distortions [11] that significantly increase the driving force for the superelastic strain. For example, the nanocomposite NiTi requires over 1 GPa stress to achieve 2% strain [10].

In recent years, new alloys have been developed to achieve a high fatigue resistance by the phase engineering methods [12–16]. As a result, some superelastic thin films can reach 10 million cyclic fatigue life under stress-induced transformations [13, 16], some bulk alloys show extremely small thermal hysteresis [14, 17], more interestingly, some transforming functional ceramics shows singular transport properties with a high fatigue life [18–20]. The key development criteria are known as Cofactor Conditions (CC) [17] including three sub-conditions CC1-3 [14]. The CC1: $\lambda_2 = 1$ condition, where λ_2 is the middle eigenvalue of the stretch tensor $\mathbf{U} \in \mathbb{R}^{3\times3}$ [21] has a significant impact on the thermal hysteresis of phase transforming materials. The thermal hysteresis was reported to be minimized at $\lambda_2 = 1$ in many material systems such as TiNi based [14, 17, 22, 23], CuZn based [12, 24], CuAl based alloys [25–27] and Heusler alloys [28–30]. The reported experimental results show that a small deviation from $\lambda_2 = 1$ can cause a large increase of thermal hysteresis for the reversible phase transformation. Naturally, it is believed that the phase reversibility can be simultaneously enhanced as λ_2 approaches 1, which was observed in some alloys [12, 13, 22, 24, 29]. However, counter examples still exist. A superelastic alloy, $CuAl_{24}Mn_9$ [25, 31] exhibits an outstanding reversibility over 10k cycles of both tensile and compressive stress-induced transformations with λ_2 far away from 1. This suggests that the phase reversibility may not be fully entangled with the $\lambda_2 = 1$ condition, especially for the stress-induced phase transformation. The primary compatibility condition may be sufficient but not necessary to achieve high reversibility during stress-induced transformations. Figure 1 shows the stress hysteresis versus λ_2 for various martensitic alloys. The trend of stress hysteresis is clustered around $\lambda_2 = 1$ but with some scattering. It raises a question whether the $\lambda_2 = 1$ condition still dominates the phase reversibility of stress-induced transformation, especially over long-lasting mechanical cycles.

From a microstructure perspective, the CC1 condition suggests a twinless structure, i.e. the martensite forms as a single lath from the austenite through an atomically sharp interface [32]. Although this microstructure is fully compatible, it limits the morphological flexibility to accommodate non-transforming defects during the phase transformation. For a stress-induced phase transformation, the formation of martensite variants is constrained by the loading orientation. As seen from Figure 1, the stress hysteresis varies by almost a factor of two as the loading orientation changes in $Ni_{50}Ti_{50}$ ([101] vs [111]) [23] and $CuAl_{24}Mn_9$ ([001] vs [111]) [25]. It implies that the Gibbs free energy minimizers for the stress-induced phase transformation are orientation dependent, more specifically martensite variant dependent.

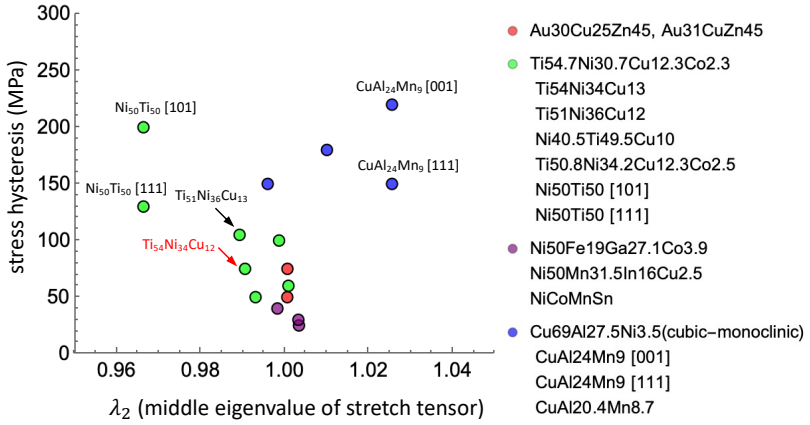

FIG. 1. Relationship between CC1: $\lambda_2 = 1$ and stress hysteresis, for CuZn based alloys from refs [12, 24] and this work, TiNi based alloys from refs [14, 17, 22, 23], Heusler alloys from refs [28–30] and CuAl based shape memory alloys from refs [25–27].

During the axial loading, the formation of martensite variant should maximize the axial strain along the loading direction, and minimize the lateral shear deformation to suppress slips. For martensitic transformation, the martensite variant can be presented by its transformation stretch tensor $\mathbf{U} \in \mathbb{R}^{3\times3}$ [21]. The CC2 condition is given by $\mathbf{Ua} \cdot \mathrm{cof}(\mathbf{U}^2 - \mathbf{I})\mathbf{n} = 0$ where the vector $\mathbf{n} \in \mathbb{R}^3$ is the twinning plane normal corresponding to the twinning shear vector $\mathbf{a} \in \mathbb{R}^3$ for the variant $\mathbf{U}$. Together with CC3: $\mathrm{tr}\mathbf{U}^2 + \det\mathbf{U}^2 - (1/4)|\mathbf{a}|^2|\mathbf{n}|^2 \leq 2$, when the material's lattice parameters satisfy the Cofactor Conditions for a specific twin system, it can achieve ultimate compatible interfaces between austenite and martensite twin laminates with variable twinning volume fractions [12, 14]. The morphology of these compatible twins is flexible, which can accommodate local non-transforming defects and nano/micro cracks. Consequently the reversibility and functional stability over loading cycles can be enhanced.

In this paper, we explore the superelasticity and functional fatigue resistance over multi-million stress-induced phase transformations of an alloy $Au_{31}Cu_{24}Zn_{45}$, belonging to the compatible alloy family [12]. The alloy development and theoretical calculations of Cofactor Conditions are provided in the Supplemental Material [33]. This alloy satisfies the CC1 condition with $\lambda_2 = 1.0067$ (not very close to 1) and CC2 condition with $\mathbf{Ua} \cdot \mathrm{cof}(\mathbf{U}^2 - \mathbf{I})\mathbf{n} = 0.000085$ (very close to 0) for $[1\bar{1}0]$ two-fold symmetry axis. For Type I/II twins with $\mathbf{n} = (1\bar{1}0)_A$, the CC3 is simultaneously satisfied by direct crystallographic calculation [34]. Therefore, the martensite phase tends to form compatible twins rather than a single variant lath. To

investigate the functional fatigue resistance, we carry out an in situ uniaxial tensile test on a T-shaped $Au_{31}Cu_{24}Zn_{45}$ micro-beam with width of 3 μm and thickness of 1.5 μm by FemtoTools Nanomechanical Testing System (model FTNMT03, Buchs ZH, Switzerland) under FEI Quanta 250 FEG Scanning Electron Microscope (SEM). We study the phase reversibility and stability of the alloy under stress-induced transformations, while observing the martensite formation and growth of structural defects. We conduct synchrotron X-ray Laue microdiffraction together with energy scans to characterize the loading orientation and precisely determine the lattice parameters of austenite and martensite near the transformation temperature at Beamline 12.3.2, Advanced Light Source, Lawrence Berkeley National Lab. Figure S2(a) in the Supplemental Materials [33] gives the orientation map, from which we determined the out-of-surface normal vector as $\mathbf{t} = [0.09822, 0.48906, 0.8667] \approx [1\,5\,9]$ in terms of the cubic basis. This is considered as the uniaxial tensile loading direction. After long cyclic fatigue tests, we study the phase interfaces, twins and the non-transforming defects at the nano to atomic scales to explore the underlying mechanisms for the million-cycle reversibility.

Figure 2 shows the transformability and reversibility of the specimen under uniaxial tensile stress induced phase transformation up to 1 million cycles. The fatigue tests were carried out at a high loading frequency of 10 Hz for the first 10^6 cycles; and at a larger loading frequency of 15 Hz up to 10^7 cycles. To minimize the effect of the thermal drift during the long-term cycling experiment, we paused the test and re-calibrated the thermal drift every 10^5 cycles for 10 Hz and 15 Hz loading rate experiments. During the first 100,000 tensile cycles, the transforming material is fully reversible. The stress-strain responses are almost identical without any nominal residual strains in Figure 2(a). The Supplementary Movie S1 shows a full superelastic cycle of the specimen under tensile stress-induced phase transformation. Based on the geometric non-linear theory of martensite with constraints [21, 24, 25, 31], we calculated the compatible twin laminates, listed in Table S1 [33], corresponding to the axial tensile strain $\epsilon_{\text{cal}} = 0.037$, which agrees with the superelastic strain, $\epsilon_t = 0.034$ measured as the plateau strain shown in Figure 2(a). The transformation stress is determined as 300 MPa with about 80 MPa stress hysteresis corresponding to 4.5% total recoverable strains without degradation up to 200k transformation cycles.

As seen in Figure 2(b), the lateral surface is clean except for several nanoscale defect hubs on the left side of the specimen, which were nucleated from the 100k-th cycle. In

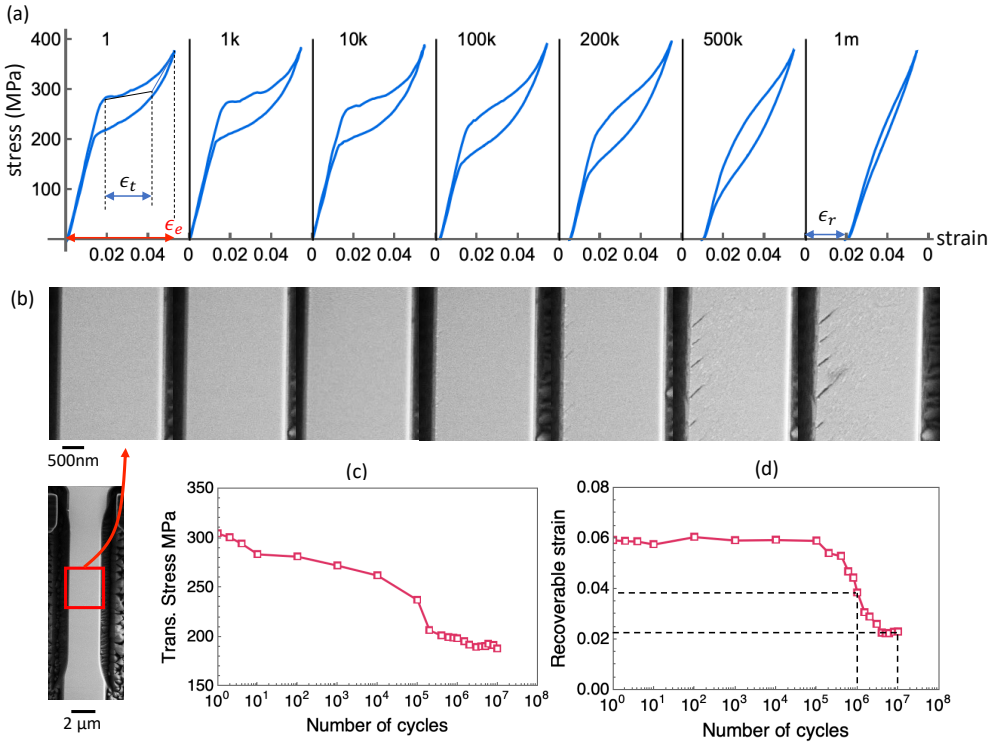

FIG. 2. The superelasticity and the growth of the nanocracks in $Au_{31}Cu_{24}Zn_{45}$ up to one million tensile stress induced phase transformations. (a) Stress-strain behaviors of the micro-beam at the 1st, 1,000th, 10,000th, 100,000th, 200,000th, 500,000th and 1 millionth mechanical cycles, corresponding to (b) the lateral surface microstructure at the maximum tensile stretch. The functional degradation of the specimen is plotted for (c) transformation stress and (d) recoverable strain (i.e. superelastic strain) over number of cycles.

subsequent tensile cycles, the specimen is loaded up to 400 MPa to complete the stress-induced transformation from austenite to martensite, then completely unloaded. Starting from the 200k-th cycle, we observed that the residual strain accumulates with increasing cycle number, while the superelastic strain and stress hysteresis are reduced. We observed that the superelastic behavior becomes less noticeable from the 500k-th to 1-millionth transformation cycles accompanied by an almost 90% decrease in stress hysteresis. Beyond this stage, we use the recoverable strain to represent the superelastic functionality. After 1 million cycles, the growth of nanocracks results in an accumulation of approximately 0.02 residual strain (denoted as ϵ_r). Despite this, the sample is still able to maintain an almost 0.04 total recoverable strain (i.e. elastic strain ϵ_e) throughout the loading and unloading pro-

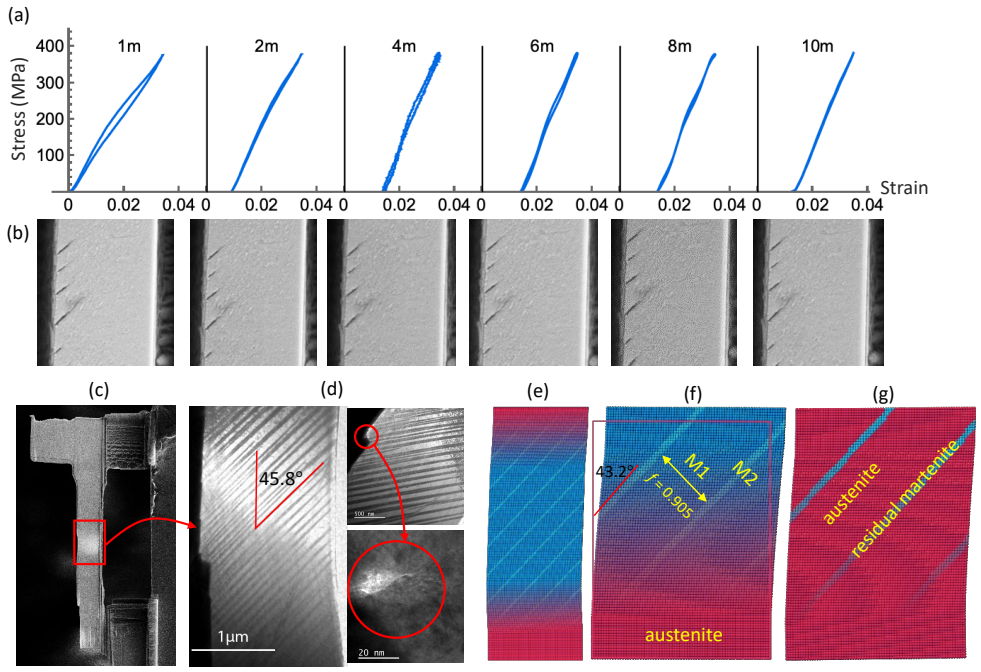

FIG. 3. The transformability and reversibility of the $Au_{31}Cu_{24}Zn_{45}$ micro-beam beyond the million mechanical cycles. (a) Stress-strain responses under the tensile loading at the 1, 2, 4, 6, 8 and 10 millionth cycles, associated with (b) the grown nanocracks on the lateral surface. (c) The TEM foil fabricated for the (d) transmission electron microscope observation of the micro-beam after 10-million mechanical cycles. (e) Prediction of the formation of the compatible twin laminates with volume fraction of 0.905. (f) Morphological configuration of the compatible interfaces among austenite, major variant M1 and minor variant M2, compared to (g) the compatible interfaces between austenite and residual martensite M2.

cess. Additionally, there is a significant reduction in stress hysteresis compared to the first cycle. The Supplementary Movie S2 shows 40 consecutive cycles of tensile stress-induced transformations after 1 million cycles. From the in situ observation of the cyclic deformations (Movie S2), the specimen is still reversible and deformable with an output of 4% recoverable strain, while no conspicuous structural defects were observed on the lateral surface of the specimen.

Beyond one million cycles, we continued the mechanical tests on the $Au_{31}Cu_{24}Zn_{45}$ micro-beam to obtain the stress-strain responses, associated with the growth of the nanocracks in Figure 3(a)-(b). From the 2-millionth cycle, the stress hysteresis became zero and the propagation of nanocracks in the specimen stopped. Figure 2(c)-(d) show that the stress-strain

behavior converges, and over 0.02 recoverable strain was achieved and stabilized beyond million cycles. Strictly speaking, the mechanical behavior at this stage is not conventionally superelastic. The transformability of the tensile specimen remains quite promising with a total one-way work of ~ 4 MJ/m^3, estimated as the bulk elastic energy gained upon loading. As a comparison, the one-way work under tensile stress in NiTi (bulk) is 10 MJ/m^3, but it degrades to 5 MJ/m^3 after only 100 cycles [6]. In magnetic shape memory alloys such as Ni_2MnGa, the one-way work in the first cycle is about 3 MJ/m^3 [35]. This suggests that the compatible alloy is still functional even after 10 millions superelastic cycles. From SEM images of Figure 3(b), the structural defects were stabilized as the same microstructure was captured at 2, 4, 6, 8,10-millionth cycles. The Supplementary Movie S3 shows 40 consecutive stress-induced transformations after 10 million cycles. The post-cycled micro-beam does not show nominal strain hardening, nor conventional slips even after numerous deformation cycles. The combination of large transformability and exceptional resilience provide a great potential for engineering applications in biomedical industries and energy science.

The post-cycled micro-beam was prepared for Transmission Electron Microscope (TEM) experiments to study the mechanism responsible for the reversibility beyond million cycles. A tiny surface step was observed on the left side where the nanocracks nucleate. It suggests that the plasticity may have initialized during the cycling history. The open crack propagated along the laminates, then was closed after traveling a 20 nm distance. Signs of crossing slip lines were not observed in this specimen. Instead, Figure 3(c)-(d) suggests the presence of residual martensite phase. Based on the compatibility theory [14, 21], we calculate the compatible twin laminates shown in Figure 3(e)-(f). The details of the calculation are given in the Supplemental Materials [33]. The calculated compatible twins consist of a major martensite variant M1 (dark blue) and a minor variant M2 (light blue) with a volume fraction 0.905 given in Figure 3(f). The transformation strain given by the minor variant of martensite is calculated as $\epsilon_{M2} = 0.0186$. Considering that about half of the region is occupied by the residual martensite (Figure 3 (d)), the minor variant M2 contributes to ~ 0.01 residual strain in the specimen. The transformation strain of the major variant M1 is $\epsilon_{M1} = 0.039$, corresponding to ~ 0.02 recoverable strain in the specimen. This calculation well agrees with the in situ nanomechanics experiment in Figure 3(a). It suggests that the minor variant is pinned while the major variant is still reversible after 10 millions of stress-induced transformation cycles.

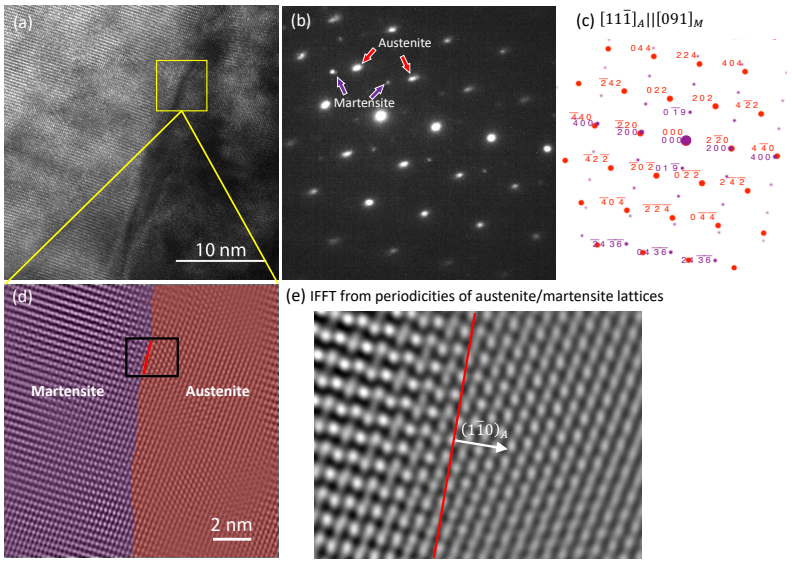

FIG. 4. (a) High resolution TEM image of the post deformed specimen near the interface between laminates. (b) The diffraction patterns from the lattices on both sides (c) indexed by austenite (red) $Fm\bar{3}m$ symmetry and martensite (purple) $P2_1$ symmetry. (d) Resolved interface morphology with a zoomed reconstructed inverse Fourier transform of the austenite/martensite lattices. (e) Lattice periodicities of austenite and martensite with an interface aligned with the twinning plane $(1\bar{1}0)_A$.

In addition, we calculated the post-cycled microstructure of the austenite and residual martensite (i.e. M2 minor variant) in Figure 3(g). The calculated deformation field and the interfaces agree with the experimental observation in Figure 3(d). In our model, there is an elastic transition layer between austenite and the twinned martensite but the lattice distortion is very small, as the CC2 condition of this twin pair is closely satisfied, i.e. CC2 = 0.00085 for both type I and II twins with the two-fold axis $[1\bar{1}0]$. The numerical details are given in Table S1 in SM [33]. The vanishing of CC2 suggests a highly coherent interface in deformed configuration between austenite and martensite through normals of type I/II twinning planes, i.e. either **n** or **Ua**. The calculated microstructure confirms such a high coherency at the austenite/M2 interface. To further verify the interface, we conducted the high-resolution TEM study (Figure 4(a)). The selected area diffraction patterns of the regions reveal that the two phases are austenite and a variant of martensite, as seen in Figure 4(b)-(c). The interface closely aligned with the $(1\bar{1}0)_A$ plane, corresponding to the

$(100)_M$ plane. The phase contrast images from the selected sub-region of Figure 4(a) were reconstructed by fast Fourier transform and inverse Fourier transform (Figure 4(e)). We can clearly distinguish two periodicities from one side (austenite) to the other (martensite), and they are not mirror-symmetry related.

In addition, the CC2 condition ensures the flexibility of twin laminates morphology, the non-transforming defects can be accommodated during the stress-induced transformation. In both pre and post cycled specimen, the dislocation density is very low, verified by the TEM observations in Figure 3(c)-(d), 4(a) and Figure S3 in the Supplemental Material. The highly coherent interfaces satisfying the CC2 condition stabilize the nanocracks and other non-transforming defects. Beyond sufficiently many deformation cycles, the phase transformation has become non-dissipative. The observed residual strain is primarily attributed to the minor martensite variant. The rest austenite region is still reversible because of the highly coherent and compatible interfaces between austenite and martensite. No further degradation will occur beyond this stage.

To conclude, we compared the recoverable strains of various transforming alloys under stress induced transformations in Figure 5. Overall, the fatigue resistance of alloys under tension is much lower than that under compression, while the achieved recoverable strains induced by tension are higher than by compression. The tensile loading is an effective actuation force but is too demanding on superelastic alloys. In Figure 5(a), the cycle-number dependent property (i.e. recoverable strain) is overlaid by the maximum applied stress contours. The recoverable tensile strains of most superelastic alloys are about 4%. They can survive 1k $\sim$ 100k transformation cycles at 200-300 MPa applied stress. The compatible $Au_{31}Cu_{24}Zn_{45}$ alloy demonstrates the recoverable strain of 4% after 1-million cycles, and 2% beyond 10-million cycles. Note that this alloy was tested at a miniature size, in which the dislocations and non-transforming defects can easily slip across the specimen. But they are suppressed by the pinned martensite minor variant. A compatible superelastic thin film [13] was reported to show a comparable functional fatigue resistance, with less than 2% recoverable strain. In the benchmark of functional fatigue resistance under compression in Figure 5(b), the compatible $Au_{30}Cu_{24}Zn_{45}$ delivers the outstanding recoverable strain of 7% even after 10^5 transformation cycles with no sign of functional degradation.

Through this comparison, we conjecture that the microstructure compatibility plays an unprecedented role in enhancing the reversibility of stress-induced phase transformation

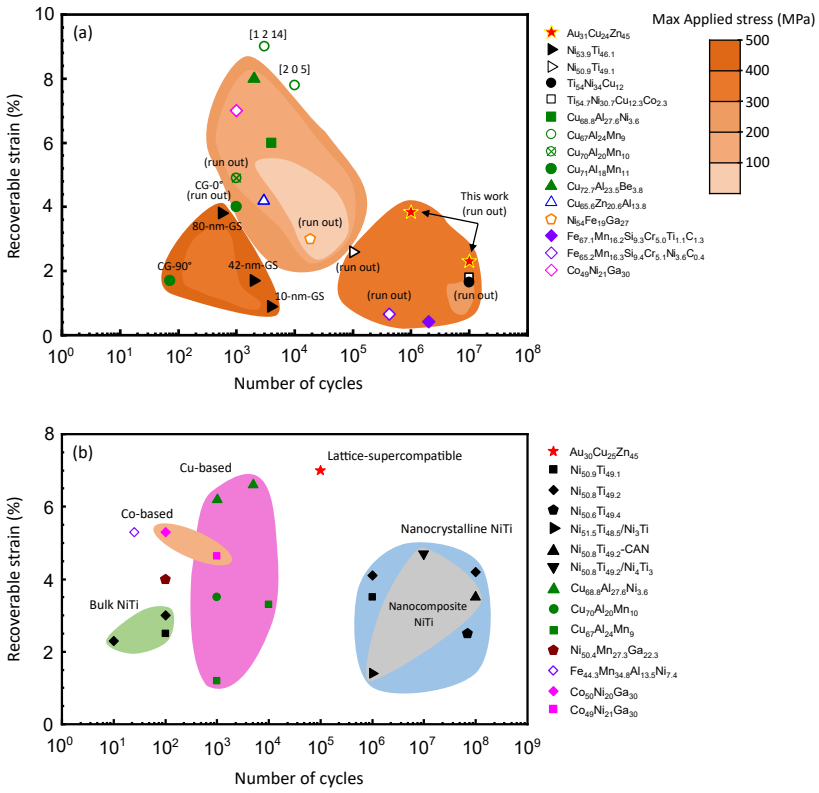

FIG. 5. Comparison of the cycle-number dependent recoverable strain under (a) tension and (b) compression among common superelastic alloys such as NiTi based alloys [7, 8, 10, 13, 36–43], CuAl and CuZn based alloys [8, 25, 31, 44–48], FeNi-based alloys [49–53], AuCuZn alloys [24]. In (a), the contours of maximum applied stress during tensile cycling are overlaid. In (a) and (b): CG-0° and CG-90° stand for the columnar-grained tensile samples oriented in 0 and 90° to the solidification direction, respectively; GS refers to the grain size; and CAN stands for crystalline-amorphous nanocomposite. The details of the alloys and their corresponding references are listed in Supplementary Tables S2 and S3.

without causing strain hardening. Particularly, the satisfaction of the Cofactor Condition CC2: $\mathbf{Ua} \cdot \mathrm{cof}(\mathbf{U}^2 - \mathbf{I})\mathbf{n} = 0$ allows for the compatible austenite and twinned martensite during the phase transformation. Moreover, it makes the lattice distortion in the elastic transition layer sufficiently small between austenite and residual martensite, stabilizing the non-transforming defect over the demanding deformation cycles. Beyond sufficient number of cycles, the phase transformation becomes non-dissipative. The non-dissipative nature of the stress-induced phase transformation under prolonged cycling ensures the exceptional resilience while maintaining the superelastic performance. Our findings provide a rational

foundation for the design of superelastic materials for biomedical applications and energy science.

M. K., Z. Z., K. H. C. and X. C. thank the financial support under GRF Grants 16203021 and 16204022 by Research Grants Council, Hong Kong. M.K., Z. Z. P. H. and X. C., thank the financial support under CRF Grant No. C6016-20G-C by Research Grants Council, Hong Kong. This research used beamline 12.3.2, a resource of the Advanced Light Source, which is a DOE Office of Science User Facility under contract no. DE-AC02-05CH11231.

* xianchen@ust.hk

[1] K. Bhattacharya and R. D. James, The Material is the Machine, Science **307**, 53 (2005).

[2] T. Yoneyama and S. Miyazaki, *Shape memory alloys for biomedical applications* (Elsevier, 2008).

[3] A. Biesiekierski, J. Wang, M. A. H. Gepreel, and C. Wen, A new look at biomedical Ti-based shape memory alloys, Acta Biomaterialia **8**, 1661 (2012).

[4] E. Bonnot, R. Romero, L. Mañosa, E. Vives, and A. Planes, Elastocaloric effect associated with the martensitic transition in shape-memory alloys, Physical Review Letters **100**, 125901 (2008).

[5] L. Mañosa and A. Planes, Materials with giant mechanocaloric effects: cooling by strength, Advanced Materials **29**, 1603607 (2017).

[6] S. Miyazaki, T. Imai, Y. Igo, and K. Otsuka, Effect of cyclic deformation on the pseudoelasticity characteristics of Ti-Ni alloys, Metall. Trans. A **17A**, 115 (1986).

[7] K. Otsuka and X. Ren, Physical metallurgy of Ti–Ni-based shape memory alloys, Progress in Materials Science **50**, 511 (2005).

[8] M. Karami and X. Chen, Nanomechanics of shape memory alloys, Materials Today Advances **10**, 100141 (2021).

[9] P. Hua, K. Chu, F. Ren, and Q. Sun, Cyclic phase transformation behavior of nanocrystalline NiTi at microscale, Acta Materialia **185**, 507 (2020).

[10] P. Hua, M. Xia, Y. Onuki, and Q. Sun, Nanocomposite NiTi shape memory alloy with high strength and fatigue resistance, Nature Nanotechnology **16**, 409 (2021).

[11] H. Chen, Y.-D. Wang, Z. Nie, R. Li, D. Cong, W. Liu, F. Ye, Y. Liu, P. Cao, F. Tian,

X. Shen, R. Yu, L. Vitos, M. Zhang, S. Li, Z. Xiaoyu, H. Zheng, J. F. Mitchell, and Y. Ren, Unprecedented non-hysteretic superelasticity of [001]-oriented nicofega single crystals, Nature materials **19**, 712 (2020).

[12] Y. Song, X. Chen, V. Dabade, T. W. Shield, and R. D. James, Enhanced reversibility and unusual microstructure of a phase-transforming material, Nature **502**, 85 (2013).

[13] C. Chluba, W. Ge, R. Lima de Miranda, J. Strobel, L. Kienle, E. Quandt, and M. Wuttig, Ultralow-fatigue shape memory alloy films, Science **348**, 1004 (2015).

[14] X. Chen, V. Srivastava, V. Dabade, and R. D. James, Study of the cofactor conditions: conditions of supercompatibility between phases, Journal of the Mechanics and Physics of Solids **61**, 2566 (2013).

[15] J. Cui, Y. S. Chu, O. O. Famodu, Y. Furuya, J. Hattrick-Simpers, R. D. James, A. Ludwig, S. Thienhaus, M. Wuttig, Z. Zhang, *et al.*, Combinatorial search of thermoelastic shape-memory alloys with extremely small hysteresis width, Nature Materials **5**, 286 (2006).

[16] H. Gu, L. Bumke, C. Chluba, E. Quandt, and R. D. James, Phase engineering and supercompatibility of shape memory alloys, Materials Today **21**, 265 (2018).

[17] Z. Zhang, R. D. James, and S. Müller, Energy barriers and hysteresis in martensitic phase transformations, Acta Materialia **57**, 4332 (2009).

[18] J. Jetter, H. Gu, H. Zhang, M. Wuttig, X. Chen, J. R. Greer, R. D. James, and E. Quandt, Tuning crystallographic compatibility to enhance shape memory in ceramics, Physical Review Materials **3**, 093603 (2019).

[19] Y. Liang, S. Lee, H. Yu, H. Zhang, Y. Liang, P. Y. Zavalij, X. Chen, R. D. James, L. A. Bendersky, A. V. Davydov, *et al.*, Tuning the hysteresis of a metal-insulator transition via lattice compatibility, Nature Communications **11**, 1 (2020).

[20] C. Zhang, Z. Zeng, Z. Zhu, N. Tamura, and X. Chen, Energy conversion from heat to electricity by highly reversible phase-transforming ferroelectrics, Physical Review Applied **16**, 024064 (2021).

[21] J. M. Ball and R. D. James, Fine phase mixtures as minimizers of energy, Arch. Rational Mech. Anal. **100**, 13 (1987).

[22] R. Zarnetta, R. Takahashi, M. L. Young, A. Savan, Y. Furuya, S. Thienhaus, B. Maaß, M. Rahim, J. Frenzel, H. Brunken, *et al.*, Identification of quaternary shape memory alloys with near-zero thermal hysteresis and unprecedented functional stability, Advanced Functional

Materials **20**, 1917 (2010).

[23] R. Manjeri, S. Qiu, N. Mara, A. Misra, and R. Vaidyanathan, Superelastic response of [111] and [101] oriented niti micropillars, Journal of Applied Physics **108** (2010).

[24] X. Ni, J. R. Greer, K. Bhattacharya, R. D. James, and X. Chen, Exceptional resilience of small-scale $Au_{30}Cu_{25}Zn_{45}$ under cyclic stress-induced phase transformation, Nano Letters **16**, 7621 (2016).

[25] M. Karami, Z. Zhu, Z. Zeng, N. Tamura, Y. Yang, and X. Chen, Two-tier compatibility of superelastic bicrystal micropillar at grain boundary, Nano Letters **20**, 8332 (2020).

[26] N. Zarubova and V. Novák, Phase stability of cualmn shape memory alloys, Materials Science and Engineering: A **378**, 216 (2004).

[27] R. D. James and Z. Zhang, A way to search for multiferroic materials with "unlikely" combinations of physical properties, in *Magnetism and Structure in Functional Materials*, edited by A. Planes, L. Mañosa, and A. Saxena (Springer Berlin Heidelberg, 2005) pp. 159–175.

[28] V. Srivastava, X. Chen, and R. D. James, Hysteresis and unusual magnetic properties in the singular heusler alloy $Ni_{45}Co_5Mn_{40}Sn_{10}$, Applied Physics Letters **97**, 014101 (2010).

[29] D. Zhao, J. Liu, X. Chen, W. Sun, Y. Li, M. Zhang, Y. Shao, H. Zhang, and A. Yan, Giant caloric effect of low-hysteresis metamagnetic shape memory alloys with exceptional cyclic functionality, Acta Materialia **133**, 217 (2017).

[30] Y. Li, D. Zhao, J. Liu, S. Qian, Z. Li, W. Gan, and X. Chen, Energy-efficient elastocaloric cooling by flexibly and reversibly transferring interface in magnetic shape-memory alloys, ACS Applied Materials and Interfaces **10**, 25438 (2018).

[31] M. Karami, K. Chu, Z. Zhu, Z. Wang, Q. Sun, M. Huang, and X. Chen, Orientation-dependent superelasticity and fatigue of cualmn alloy under in situ micromechanical tensile characterization, Journal of the Mechanics and Physics of Solids **160**, 104787 (2022).

[32] R. Delville, S. Kasinathan, Z. Zhang, J. V. Humbeeck, R. D. James, and D. Schryvers, Transmission electron microscopy study of phase compatibility in low hysteresis shape memory alloys, Philosophical Magazine **90**, 177 (2010).

[33] See Supplemental Material at [URL will be inserted by publisher] for Materials and Methods, Compatibility conditions of austenite/martensite interfaces, Algorithm for austenite/martensite interfaces, Figures S1 - S4, Tables S1 - S3, Captions of Movies S1 - S3. The Supplemental Material also contains Refs. [8-13, 25-27, 30, 35, 36, 39-52].

[34] M. Chapman, M. De Graef, R. D. James, and X. Chen, Quantitative analysis of compatible microstructure by electron backscatter diffraction, Philosophical Transactions of the Royal Society A **379**, 20200112 (2021).

[35] I. Karaman, H. E. Karaca, B. Basaran, D. C. Lagoudas, Y. I. Chumlyakov, and H. J. Maier, Stress-assisted reversible magnetic field-induced phase transformation in Ni_2MnGa magnetic shape memory alloys, Scripta Mater. **55**, 403 (2006).

[36] H. Yin, Y. He, Z. Moumni, and Q. Sun, Effects of grain size on tensile fatigue life of nanostructured NiTi shape memory alloy, International Journal of Fatigue **88**, 166 (2016).

[37] J. Tušek, A. Žerovnik, M. Čebron, M. Brojan, B. Žužek, K. Engelbrecht, and A. Cadelli, Elastocaloric effect vs fatigue life: Exploring the durability limits of Ni-Ti plates under pre-strain conditions for elastocaloric cooling, Acta Materialia **150**, 295 (2018).

[38] R. Sidharth, A. Mohammed, and H. Sehitoglu, Functional fatigue of niti shape memory alloy: Effect of loading frequency and source of residual strains, Shape Memory and Superelasticity , 1 (2022).

[39] H. Lin, P. Hua, K. Huang, Q. Li, and Q. Sun, Grain boundary and dislocation strengthening of nanocrystalline NiTi for stable elastocaloric cooling, Scripta Materialia **226**, 115227 (2023).

[40] P. Hua, H. Lin, and Q. Sun, Ultrahigh cycle fatigue deformation of polycrystalline NiTi micropillars, Scripta Materialia **203**, 114108 (2021).

[41] J. Chen, K. Zhang, Q. Kan, H. Yin, and Q. Sun, Ultra-high fatigue life of NiTi cylinders for compression-based elastocaloric cooling, Applied Physics Letters **115**, 093902 (2019).

[42] H. Hou, E. Simsek, T. Ma, N. S. Johnson, S. Qian, C. Cissé, D. Stasak, N. Al Hasan, L. Zhou, Y. Hwang, *et al.*, Fatigue-resistant high-performance elastocaloric materials made by additive manufacturing, Science **366**, 1116 (2019).

[43] F. Xiao, K. Chu, Z. Li, R. Hou, Y. Gao, Q. Sun, and X. Jin, Improved functional fatigue resistance of single crystalline NiTi micropillars with uniformly oriented Ti_3Ni_4 precipitates, International Journal of Plasticity **160**, 103480 (2023).

[44] J. Liu, H. Huang, and J. Xie, Superelastic anisotropy characteristics of columnar-grained Cu–Al–Mn shape memory alloys and its potential applications, Materials & Design **85**, 211 (2015).

[45] C. Qiu and S. Zhu, Characterization of cyclic properties of superelastic monocrystalline Cu–Al–Be sma wires for seismic applications, Construction and Building Materials **72**, 219 (2014).

[46] S. M. Ueland and C. A. Schuh, Superelasticity and fatigue in oligocrystalline shape memory alloy microwires, Acta materialia **60**, 282 (2012).

[47] J. F. Gómez-Cortés, M. L. Nó, I. Ruíz-Larrea, T. Breczewski, A. López-Echarri, C. A. Schuh, and J. M. San Juan, Ultrahigh superelastic damping at the nano-scale: A robust phenomenon to improve smart MEMS devices, Acta Materialia **166**, 346 (2019).

[48] J. San Juan, J. Gómez-Cortés, G. López, C. Jiao, and M. Nó, Long-term superelastic cycling at nano-scale in Cu-Al-Ni shape memory alloy micropillars, Applied Physics Letters **104**, 011901 (2014).

[49] C. Efstathiou, H. Sehitoglu, P. Kurath, S. Foletti, and P. Davoli, Fatigue response of NiFeGa single crystals, Scripta Materialia **57**, 409 (2007).

[50] K. N. Hong, Y. M. Yeon, W. B. Shim, and S. W. Ji, Fatigue characteristics of Fe-based shape-memory alloys, Applied Sciences **10**, 5812 (2020).

[51] P. Krooß, T. Niendorf, P. Kadletz, C. Somsen, M. Gutmann, Y. Chumlyakov, W. W. Schmahl, G. Eggeler, and H. Maier, Functional fatigue and tension–compression asymmetry in [001]-oriented $Co_{49}Ni_{21}Ga_{30}$ high-temperature shape memory alloy single crystals, Shape Memory and Superelasticity **1**, 6 (2015).

[52] L. Wei, X. Zhang, J. Liu, and L. Geng, Orientation dependent cyclic stability of the elastocaloric effect in textured Ni-Mn-Ga alloys, AIP Advances **8**, 055312 (2018).

[53] A. Shen, D. Zhao, W. Sun, J. Liu, and C. Li, Elastocaloric effect in a $Co_{50}Ni_{20}Ga_{30}$ single crystal, Scripta Materialia **127**, 1 (2017).